

Effect of the Exposure Time in Laser Speckle Imaging for Improving Blood Vessels Localization: a Wavelet Approach

F. Lopez-Tiro, H. Peregrina-Barreto, J. Rangel-Magdaleno, J. C. Ramirez-San-Juan, J. M. Ramirez-Cortes

Instituto Nacional de Astrofísica, Óptica y Electrónica

Luis Enrique Erro 1, Santa Maria Tonantzintla, 72840. Puebla, México

Corresponding author: hperegrina@inaoep.mx

Abstract—The visualization and localization of blood vessels in Laser Speckle Contrast Imaging is an important task to determine the presence of blood vessels in the biological tissue. However, Laser Speckle Contrast Imaging has some drawbacks when the depth of the blood vessels increases. This work establishes a methodology based on a wavelet approach to improve the localization of blood vessels in *in-vitro* contrast images. It also determines a useful exposure time to improve the localization of blood vessels. The results show that the wavelet approach allows blood vessels to be located up to $510\mu\text{m}$ deep under a skin phantom. In addition, it states that high exposure times increase the percentage of similarity in traditional models and visualization enhancement models.

Keywords: Exposure time, Laser Speckle Contrast Imaging, Localization of blood vessels, Wavelet Approach.

I. INTRODUCTION

The visualization and localization of blood vessels is a fundamental task in the assessment of the state and health of biological tissues such as skin [1], retina [2], brain [3] among others. Laser Speckle Imaging (LSI) is an effective technique for measuring blood flow in superficial blood vessels through the analysis of LSI images [4], [5]. The movement of particles in the blood flow, such as red blood cells, produces a blurring effect on the LSI image that is associated to the localization of a blood vessel [6], [7]. The contrast computation based on LSI is known as Laser Speckle Contrast Imaging (LSCI) and improves the blood vessel visualization and localization. However, the visualization in LSCI is limited by the the blood vessels depth in the tissue [8]. As the depth increases, the visualization of blood vessels is reduced since the noise level is higher. To solve this problem, a set of techniques based on physical, instrumental, and computational improvements have been proposed [9].

Physical improvements made during the acquisition of speckle images have had good results in improving the visualization of blood vessels [10]–[12]. However, these techniques turn out to be slightly invasive, since they involve the use of external agents in the skin or introduce particles foreign to the blood flow; these methods could be not adequate in sensitive regions such as retina or brain. The instrumental improvements made before and during the acquisition of speckle images are non-invasive techniques for calculating and correcting the effect of scattering with a single exposure time [13]. However, it is limited when the depth of scattering in the sample is high. Computational improvements to LSI images have obtained favorable results through different approaches. On the one hand, traditional approaches based on contrast representation (LSCI) allows the visualization of superficial blood vessels and the relative blood flow calculation [14]. On the other hand, new approaches have been developed for improving the visualization and localization of blood vessels at higher depths from the analysis of the digital image [16]–[24]. However, computational

improvements still have some limitations because the noise in the sample increases with depth.

The proposed methodology studies two aspects: (i) the exposure time effect on contrast is analyzed to improve the blurring effect during the acquisition of speckle images, and (ii) the visualization of blood vessels is improved by an approach based on the decomposition of the discrete wavelet transform (DWT). Finally, a comparison is made between the contrast calculated with a traditional approach and a contrast enhancement through an approach based on the Discrete Wavelet Transform. Both approaches were tested at different exposure times. The experimental results of the proposed approach show that it is possible to improve the visualization of blood vessels in LSCI images when the exposure time is high. Also, the exposure time is useful for calculating contrast, as well as for improving the visualization of superficial and deep blood vessels.

II. CONCEPTS

A. Speckle

The speckle phenomenon occurs when the photons of a coherent light laser interact with a rough surface generating scattering of photons off the surface. An optical detector integrates into an image the constructive and destructive interference caused by the scattering of photons. The acquired image is a pattern of dark and bright spots known as the speckle pattern (Fig. 1a). The absence or presence of particle movement within the surface can cause two effects on the speckle image. On the one hand, the absence of motion over time is known as static speckle. On the other hand, the presence of time-varying motion produces a blurred effect and is known as dynamic speckle, the analysis of this effect is the basis of LSI [7].

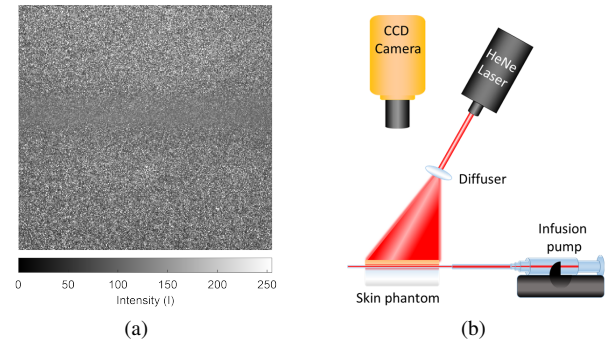


Fig. 1: (a) LSI image of a *in-vitro* straight blood vessel at $0\mu\text{m}$ depth, the central blurring pattern corresponds to the blood vessel, (b) experimental setup that acquires the images of (a).

B. Experimental setup

The experimental setup (Fig. 1b) consists of an He-Ne Laser (632.8nm) which homogeneously illuminates a skin phantom using

an optical diffuser (*Model ED1 - C20, Thorlabs Inc*) as shown in Fig. 1b. A package of images of speckle is acquired by a CCD camera (*Model Retiga2000R, QImaging, Canada*) equipped with a macro lens. The skin phantom was manufactured with optical properties (scattering coefficient) similar to human skin, as reported in [25]. Two phantoms were used: one for the epidermis and one for the dermis. Different epidermis layer thicknesses from $0\mu\text{m}$ to $1000\mu\text{m}$ were used. To simulate the blood vessels of the skin phantom, we used a straight glass capillary with an inside diameter of $700\mu\text{m}$ (*thinXXS Microtechnology AG, Germany*) located on the surface of the dermis. The infusion of intralipids at 3% in water was used to simulate the scattering properties of human blood and pumped through the capillaries with a pump (*Model NE-500, NewEraPumpSystemInc*), controlled the blood flow.

C. Contrast

The analysis of LSI images is commonly studied through a contrast representation. When a set of LSI images (raw) is processed to calculate contrast, a contrast image or LSCI image is obtained [14].

Several approaches have been used to calculate the contrast K which is defined as the relationship between the standard deviation ($\sigma(W)$) and the average intensity ($\bar{I}(W)$), where W is an analysis window centered on the (x,y) coordinates that slides through the LSI image for computing contrast [9]. By definition, contrast values are between $[0,1]$. Values close to 0 indicate low contrast and correspond to the dynamic speckle (blood vessel). On the other hand, values close to 1 indicate high contrast and are related to the static speckle (skin tissue) [8].

$$K(x,y) = \frac{\sigma(W)}{\bar{I}(W)} \quad (1)$$

One of the most common approaches is the spatial contrast (sK) which attenuates noise by considering neighborhood information within a spatial analysis window $W_{d \times d}^{sK}$, where d is the size of the window. sK provides a representation with improved noise attenuation.

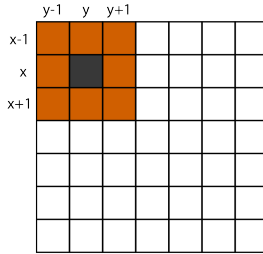


Fig. 2: Pixels used to calculate contrast with an analysis window $d = 3$ for spatial contrast. The orange squares are part of the analysis window, the black square represents the central pixel.

A variant of sK is the spatial contrast averaged denoted as sK_{avg} . sK_{avg} calculates the average of a set of N spatial LSCI images (1) for each pixel located in the coordinates (x,y) as shown in (2):

$$sK_{avg}(x,y) = \frac{1}{N} \sum_{i=1}^N sK(x,y)(i) \quad (2)$$

sK_{avg} maintains a high spatial resolution of the contrast values at the cost of the temporal resolution improving the blood vessel visualization.

D. Wavelet Transform

The Wavelet Transform (WT) is a technique for local analysis of non-stationary and fast-changing signals and images. WT provides multi-resolution analysis with expanded windows. The wavelet

domain is a useful tool in noise attenuation since it provides a more accurate spatial and spectral decomposition respect to other techniques such as Fourier Transform (FT) [26]–[28]. The implementation of the WT for discrete values is known as the Discrete Wavelet Transform (DWT) and can be interpreted as a process of analysis and synthesis for multiple levels of filtering. A level of analysis denoted as j can take multiple integer values from 1 up to a maximum filtering level of J of a signal or image [29].

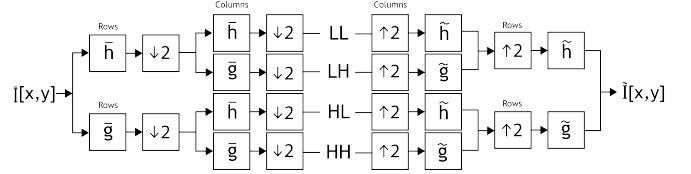


Fig. 3: DWT implementation as a filter bank for the first level of decomposition. Analysis (left) and synthesis (right) of image $\tilde{I}(x,y)$ through decomposition filters ($\tilde{h}[k]$ and $\tilde{g}[k]$) and reconstruction ($\tilde{h}[k]$ and $\tilde{g}[k]$).

1) *Analysis*: In digital images, the DWT analysis process filters spatial information from an image $\tilde{I}(x,y)$ with a size of $M \times N$ through the high-pass $\tilde{h}[k]$ and low-pass $\tilde{g}[k]$ filters defined by a wavelet function ψ , where $[k]$ is the number of coefficients that describe the filter [30], [31]. After filtering, it goes through a subsampling process $\lfloor \downarrow 2$ where the image dimensions are reduced by a scale of 2^j in the x direction of the image. Then, the same process is repeated in the y direction of the image. The result of the DWT analysis process is the approximation coefficients (LL_j) and detail (LH_j, HL_j, HH_j) for the filter level j with dimensions $M/2^j \times N/2^j$. The approximation coefficients (LL_j) correspond to the low-frequency information from 0 to $\pi/2^j$, given by the low pass filters $\tilde{g}[k]$, while the horizontal detail coefficients (LH_j), vertical (HL_j), and diagonal (HH_j) correspond to the high-frequency information from $\pi/2^j$ to π , given by the combination of filters $\tilde{g}[k]$ and $\tilde{h}[k]$. The result of the DWT decomposition process can be seen on the left side of Fig. 3.

2) *Synthesis*: The DWT synthesis process is the reverse of the DWT analysis process. In the DWT synthesis process given a filtering level of $j \geq 1$, it allows to assemble the information of the coefficients (LL_j, HL_j, LH_j, HH_j) through the processes of oversampling [2] and filtering through the synthesis filters $\tilde{g}[k]$ and $\tilde{h}[k]$. In image filtering, the DWT synthesis process is generally used to assemble the approximation coefficient information (LL_j) of size $M/2^j \times N/2^j$, while detail coefficients are processed as empty element coefficients that only retain the size of the coefficient. This process allows you to attenuate the noise of the detail coefficients and retrieve a filtered or synthesized image $\tilde{I}[x,y]$ dimensions $M \times N$ with low-frequency information of 0 to $\pi/2^j$. The result of the DWT synthesis process can be seen on the right side of Fig. 3.

E. Clustering

The k -means grouping algorithm is unsupervised and is used to segment the area of interest. It groups or divides the given data into k groups or parts based on the k -centroids. The algorithm is used when it has unlabeled data like data without defined categories or groups. The goal is to find certain groups based on some kind of similarity in the data with the number of groups represented by k . The goal of k -means grouping is to minimize the sum of the square distances between all points and the center of the group.

$$C_k = \sum_{a=1}^k \sum_{b=1}^n \|p_b^{(a)} - c_a\|^2 \quad (3)$$

Where k is the number of clusters, n is the number of classes, p_b is the case b and the pixel with coordinates (x,y) analyzed, c_a is the centroid of cluster a , and C_k is the objective function that provides a quantized image of k clusters [32].

III. METHODOLOGY

The present study is based on three assumptions: The first assumption states that speckle images are made up of two regions of interest: dynamic speckle related to the movement of particles in blood vessels and static speckle associated with biological tissue such as skin. The second assumption states that the exposure time used when acquiring speckle images has a positive and negative effect on the blurred of the dynamic speckle. The third assumption is that the frequency range of the LSCI image is from 0 to π . Where the values near 0 correspond to the low frequencies, and the values near π correspond to the high frequencies.

Therefore, in this methodology we study the effect that exposure time has on the calculation of contrast in blood vessels at different depths, and a constant flow velocity along the blood vessel. On the one hand, the effect of exposure time is studied in traditional approaches such as sK . On the other hand, the effect of exposure time is studied through the wavelet approach as a model to improve the visualization of blood vessels in LSCI images denoted as $\tilde{I}(x,y)$.

A. Denoising

Under the assumption that LSCI image values are noisier as depth increases and presents a frequency spectrum between 0 and π with high and low-frequency information, DWT analysis and synthesis processes are used to attenuate noise in LSCI images. The DWT analysis process (Sec. II-D.1) consists of denoising the LSCI image $\tilde{I}(x,y)$ in order to obtain a new representation of the LSCI image with a low amount of noise, avoiding the fusion of information between the dynamic and static speckle. The parameters used to perform the DWT analysis process are a wavelet function denoted as ψ and a filtering level denoted as j . The filtering process is performed on the approximation coefficients without considering the information of the detail coefficients. The result of the DWT analysis process for the j level are the approximation coefficients (LL_j) and detail (LH_j, LH_j, LH_j). Where, the approximation coefficients (LL_j) correspond to a LSCI image with attenuated noise of dimensions $M/2^j \times N/2^j$ and has a low-frequency spectrum from 0 to $\pi/2^j$. To obtain an image of the original size, the DWT synthesis process of the approximation coefficients is performed at the j level, described in Sec. II-D.2. As a result of the DWT synthesis process, we get a synthesized image $\tilde{I}(x,y)$ with dimensions $M/2^{j=0} \times N/2^{j=0}$ and a low-frequency spectrum from 0 to $\pi/2^j$.

B. Clustering

Under the assumption that the new contrast values in a synthesized image (Fig. 4b) are a low-frequency representation with a spectrum from 0 to $\pi/2^j$ due to attenuated noise after the DWT analysis and synthesis processes; it is possible to establish two classes after DWT process: dynamic speckle, and static speckle, denoted as C_1 , and C_2 respectively, through of a clustering method such as k -means clustering based image segmentation. The result is a binary image in two classes $[0, 1]$ (Fig. 5a). The dynamic speckle is denoted as 1, while the static speckle is 0.

After the clustering process, small isolated particles and rough edges usually appear around the dynamic speckle. To reduce the isolated particles, an area criterion is used to remove those particles that are not considered part of the dynamic speckle. The area criterion orders the elements labeled in the binary image as 1 from the largest to the smallest area (number of skins). Then, it selects the element with the largest area and converts all the other elements of the image to 0. The result of the area criterion is a new binary image denoted as $I_{bin}(x,y)$ of two classes $[0, 1]$ (Fig. 5b). The dynamic speckle is denoted as 1, while the static speckle is 0.

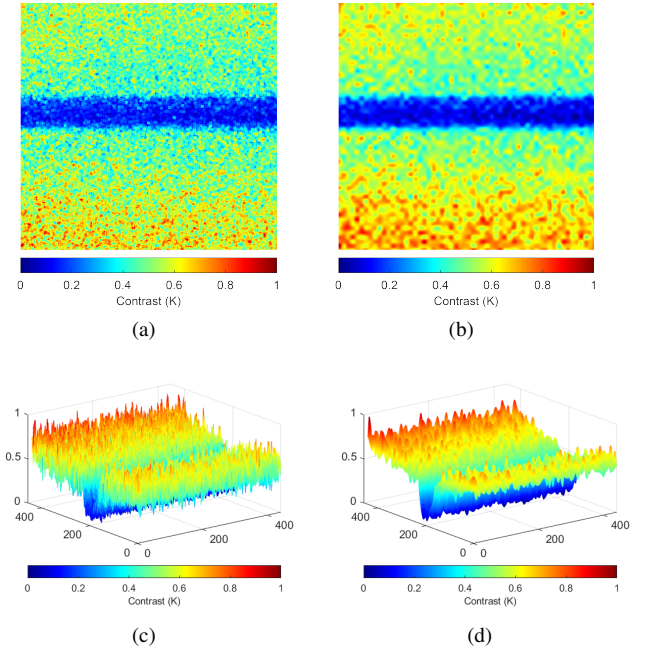


Fig. 4: (a) *In-vitro* LSCI image, (b) its synthesis with DWT after $j=5$ levels of decomposition; (c, d) their respective lateral views.

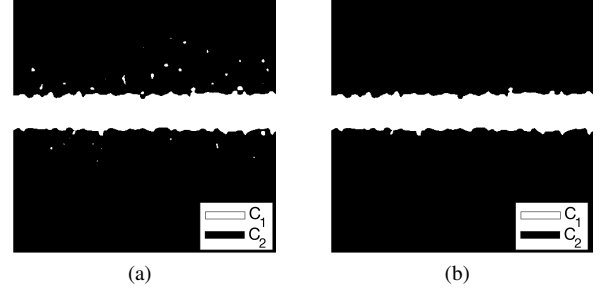


Fig. 5: (a) Binarization process; (a) binarized image from clustering method with k , and (b) binarized image after applying an area criterion.

IV. RESULTS

A. Data set

The speckle image set consists of 75 image packs, each containing 30 speckle images of *in-vitro* straight blood vessels. The set of speckle images were obtained by the experimental setup described in Sec. II-B. The exposure time of the blood vessels is denoted as T and take 15 average values of 70.60ms, 138.40ms, 256.60ms, 500ms, 980.20ms, 1883.40ms, 3949.60ms, 5908.60ms, 8204.80ms, 11062ms, 12200.60ms, 20885.00ms, 26481.80ms, 31760ms and 32789.80ms. The depths of the blood vessels is denoted as ρ are $0\mu m, 190\mu m, 311\mu m, 510\mu m$ and $1000\mu m$. The dimensions of the *in-vitro* images for straight blood vessels are 640×480 pixels. The ground truth (GT) was obtained by tagging the blood vessel to a depth of $0\mu m$. The labeling is a binary image consisting of two classes $[0, 1]$. The dynamic speckle class labeled as 1, while the static speckle label is 0. GT was used to evaluate depths between $0\mu m$ and $1000\mu m$. The LSCI images used to evaluate this model were computed with the averaged spatial contrast algorithm (2) from the set of speckle images described in Sec. IV-A.

TABLE I: Performance of similarity measured with RI of the depths $\rho = \{0\mu m, 190\mu m, 311\mu m, 510\mu m, 1000\mu m\}$.

	0 μm		190 μm		311 μm		510 μm		1000 μm	
T [ms]	sK_{avg}	WA	sK_{avg}	WA	sK_{avg}	WA	sK_{avg}	WA	sK_{avg}	WA
70.6	45.72%	95.78%	49.89%	89.83%	52.02%	41.70%	59.09%	44.55%	59.27%	52.26%
138.40	48.50%	96.04%	50.17%	94.26%	52.44%	89.89%	59.19%	46.45%	59.53%	52.67%
256.60	54.11%	96.16%	51.06%	94.61%	52.61%	92.60%	59.23%	83.08%	62.91%	53.35%
500	59.51%	96.19%	51.32%	94.65%	52.90%	92.67%	59.29%	84.96%	63.59%	53.74%
980.20	64.72%	96.23%	52.08%	94.68%	53.53%	93.50%	59.36%	85.92%	63.93%	53.93%
1883.40	90.47%	96.26%	52.35%	94.71%	53.87%	93.61%	59.48%	86.12%	64.71%	55.26%
3949.60	95.08%	96.27%	61.20%	94.72%	54.66%	93.67%	64.84%	86.71%	64.73%	55.33%
5908.60	95.09%	96.31%	62.75%	94.73%	56.16%	93.71%	66.41%	86.85%	64.86%	55.43%
8204.80	95.60%	96.32%	83.58%	94.73%	69.24%	93.73%	69.90%	87.17%	64.97%	55.71%
11062	95.67%	96.35%	85.49%	94.85%	73.18%	93.81%	70.02%	87.53%	65.01%	55.87%
12200.60	95.87%	96.38%	88.57%	94.89%	78.21%	93.85%	74.88%	87.64%	65.67%	59.58%
20885.00	95.89%	96.43%	89.48%	95.02%	82.24%	93.87%	74.95%	87.77%	65.76%	68.87%
26481.80	96.05%	96.43%	89.70%	95.04%	82.74%	93.95%	75.53%	87.91%	66.11%	70.11%
31760	96.27%	96.46%	90.46%	95.21%	85.34%	94.04%	77.58%	88.39%	68.76%	70.30%
32789.80	96.48%	96.58%	92.06%	95.31%	85.86%	94.05%	79.06%	89.54%	70.00%	73.03%
AVG	81.67%	96.28%	70.01%	94.48%	65.67%	89.91%	67.25%	81.37%	64.65%	59.03%
Error	20.35%	0.19%	718.34%	1.31%	14.09%	13.38%	7.73%	14.65%	2.80%	7.45%

B. Settings

In general, methodologies have parameters selected by the user. In the present methodology, two parameters were selected for the wavelet approach: wavelet function ψ and filtering level j .

The wavelet function ψ was selected through a combinatorial search of functions 2 to 32 in the Symlet family. The selection criteria of ψ were the results of similarity of the binary image (Fig. 5a) and the GT of the input set (Sec. IV-A). The similarity was assessed for 31 wavelet functions and was measure with the Rand Index (RI) denoted as:

$$RI = \frac{TP + TN}{TP + TN + FP + FN} \quad (4)$$

Given two binary images A and B where 1 is the dynamic speckle and 0 is the static speckle. Where, True Positive (TP) represents the total number of pixels where A and B have a value of 1. True Negative (TN) represents the total number of pixels where A is 0 and B is 1. False Negative (FN) represents the total number of pixels where A is 1 and B is 0. False Positive (FP) represents the total number of pixels where A and B are 0. The wavelet function Symlet 5 had the highest mean value and the lowest standard deviation of the full set of wavelet functions. The RI obtained for Symlet 5 was $52.16 \pm 18.23\%$.

In the selection of the j filtering level, only the information of the approximation coefficients during the analysis process was considered. The maximum filtering level selected was level 5, $J = 5$. The levels greater than 5 were discarded, due to the $M \times N$ dimensions of the LSCI images and the number of coefficients of the selected wavelet function that limit the number of j filtering levels. The methodology was evaluated for $j = \{1 \dots J\}$ filtering levels. Using (4) the RI was calculated for each j level and the level with the best similarity performance to the GT was selected. The j level selected the selected level was 5. The RI obtained for level $j = 5$ was $84.22 \pm 16.52\%$.

TABLE II: Selection of the decomposition level j for the wavelet focus measured with RI.

Level	0	1	2	3	4	5
Average	69.85%	71.89%	72.70%	71.30%	75.80%	84.22%
Error	15.12%	15.69%	17.08%	21.10%	22.38%	16.52%

C. Performance of exposure time

One of the main drawbacks of LSCI is setting the exposure time for a particular model. On the one hand, short exposure times have the advantage of reducing the time during acquisition of an LSI image, which is convenient in a traditional LSI system at the cost of providing a reduced fading effect that reduces contrast in LSCI images. Long exposure times, on the other hand, present a high level of blur in LSI images during acquisition, which is useful in providing a high level of contrast between dynamic and static speckle, at the cost of increasing the integration time of the CCD camera.

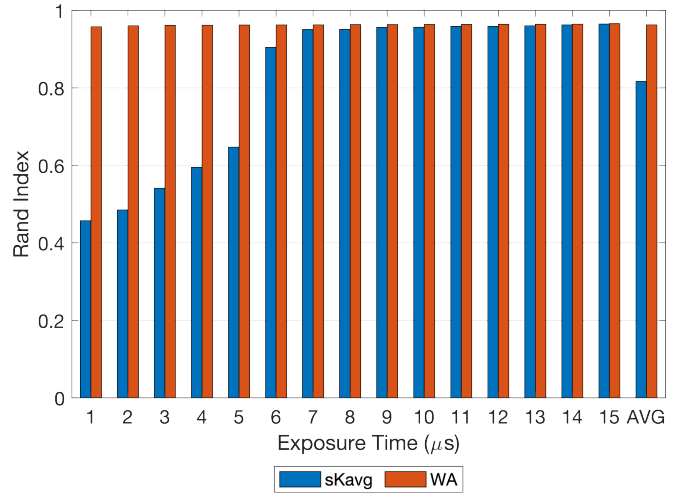


Fig. 6: Effect of the exposure time performance of the sK_{avg} and WA models for blood vessels at $0\mu m$ depth.

In order to select the appropriate exposure time for the sK_{avg} and WA models, the present methodology was tested in the set described in Sec. IV-A. The parameters used in the present methodology were for the decomposition process DWT: (i) a function wavelet ψ Symlet 5 and a filtering level $j = 5$. Usually, in the clustering process, one of the main limitations is to select the number of k clusters, since it is often a problem to determine the number of classes that a given image will have. However, for the present methodology the the clustering process used a $k = 2$ since the objective is to determine an image composed of two classes: the

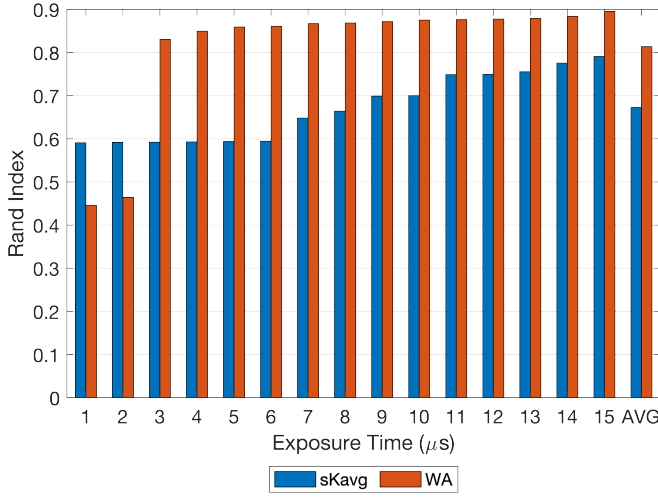


Fig. 7: Effect of the exposure time performance of the sK_{avg} and WA models for blood vessels at $510\mu m$ depth.

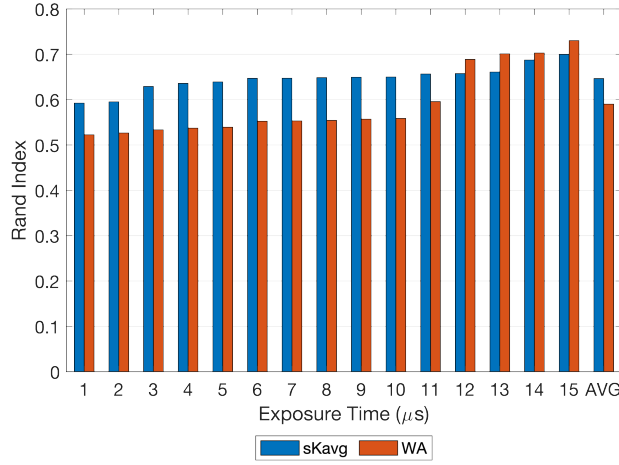


Fig. 8: Effect of the exposure time performance of the sK_{avg} and WA models for blood vessels at $1000\mu m$ depth.

dynamic and static speckle region.

Table I presents similarity performance across two models: (i) spatial contrast averaged (sK_{avg}) as a traditional model and (ii) a wavelet approach (WA) as a visualization and localization enhancement model. The performance of both models was measured with RI at 5 depths $\rho = \{0\mu m, 190\mu m, 311\mu m, 510\mu m, 1000\mu m\}$ for 15 average exposure times ordered from the lowest exposure time $T_{min} = 70.6[ms]$ to the highest exposure time $T_{max} = 32789.80[ms]$. The results suggest that long exposure times (closer to T_{max}) have the best RI performances. In sK_{avg} and WA, exposure times greater than 12200.60 ms offer better similarity performance.

In the particular case of depth $0\mu m$ for the sK_{avg} model, the recommended exposure time is any greater than the average for the set of $0\mu m$ (81.67%), i.e. $T > 1883.40[ms]$. Then, for the WA model with depth $0\mu m$, the recommended exposure time is any greater than the average of the set of $0\mu m$ (96.28%), that is $T > 5908.60[ms]$. It is important to note that in the sK_{avg} model the performance results below the recommended exposure time (1883.40 [ms]) drop from 25.75% to 44.75%. While using the WA

model the performance results less than the recommended exposure time (5908.60 [ms]) declines to 0.53%. Fig. 6 shows the behavior of both models for 15 exposure times, where the first T is 70.6 [ms] and the fifteenth is 32789.80 [ms].

In the case of depths $190\mu m$, and $311\mu m$ follow a similar behaviour for exposure time of depth $510\mu m$. In the case of the $510\mu m$ depth for the sK_{avg} model, the recommended exposure time is any greater than the average for the $510\mu m$ set (69.90%), i.e. $T > 8204.80[ms]$. Then, for the WA model with depth $510\mu m$, the recommended exposure time is any greater than the average for the $510\mu m$ set (83.08%), that is $T > 256.60[ms]$. It is important to note that in the sK_{avg} model the performance results below the recommended exposure time (8204.80 [ms]) drop from 69.90% to 59.09%. While using the WA model performance results below the recommended exposure time (256.60 [ms]) declines to 38.53%. In Fig. 7 you can see the exposure time behavior in both models.

Finally, in the case of the $1000\mu m$ depth for the sK_{avg} model, the recommended exposure time is any greater than the average for the $1000\mu m$ set (64.71%), i.e. $T > 1883.40[ms]$. Then, for the WA model with depth $1000\mu m$, the recommended exposure time is any greater than the average of the $1000\mu m$ set, i.e. $T > 12200.60[ms]$. It is important to note that in the sK_{avg} model the performance results below the recommended exposure time (1883.40 [ms]) drop from 64.71% to 59.27%. While using the WA model performance results below the recommended exposure time (12200.60 [ms]) declines to 7.32%. Fig. 8 shows the behavior of both models.

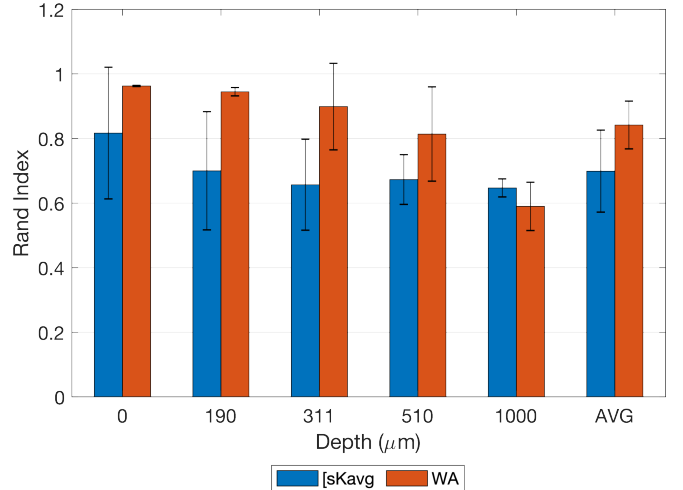


Fig. 9: Average similarity performance for depths $\rho = \{0\mu m, 190\mu m, 311\mu m, 510\mu m, 1000\mu m\}$ for sK_{avg} and WA models in blood vessels.

The Fig. 9 shows the average similarity yield for the depths $\rho = \{0\mu m, 190\mu m, 311\mu m, 510\mu m, 1000\mu m\}$ in the sK_{avg} and WA models. You can see that the WA model is superior in average similarity for blood vessels with depths up to $510\mu m$. However, the performance declines in blood vessels with depths of $1000\mu m$. On the one hand, the average yield of the sK_{avg} model is $69.85 \pm 12.66\%$ with a maximum of $81.66 \pm 20.35\%$. On the other hand, the average yield of the WA model is $84.21 \pm 7.39\%$ with a maximum of $96.27 \pm 0.19\%$. This indicates that the WA model is superior to the sK_{avg} model by $14.36 \pm 5.26\%$.

V. DISCUSSION

An important aspect to consider in *in-vivo* applications is the artifacts produced by heart rate or breathing. Unlike *in-vitro* applications, *in-vivo* images have an increase in the amount of noise due to artifacts, and consequently, the blurring of the dynamic speckle

may decrease. A first solution to the lack of blurring of *in-vivo* images is to increase the exposure time of the camera at the time of acquisition of the LSI images. Another important aspect to consider in *in-vivo* images is the size of the blood vessels. Unlike *in-vitro* images where the diameter of the blood vessels is constant, in *in-vivo* images the diameter of the blood vessels is variable. On the one hand, the major blood vessels maintain a similar diameter and a high degree of blurring due to a high amount of circulating blood cells. While in the secondary blood vessels produced by branches of the main blood vessels, they have a poor blurring caused by the low circulation of blood cells and therefore could be mistaken for tissue. A second solution for locating secondary blood vessels may be an adaptive process in regions where blurring is low.

VI. CONCLUSIONS

The visualization and localization of blood vessels in Laser Speckle Contrast Imaging is an important task to determine the presence of blood vessels in the biological tissue. However, Laser Speckle Contrast Imaging has some drawbacks when the depth of the blood vessels increases. This paper presented a methodology based on a wavelet approach to attenuate noise in LSCI images, improve the localization of blood vessels and establish a binary marker as a result of the clustering process. In addition, a useful exposure time was determined to improve the localization of blood vessels and where high exposure times increase the percentage of similarity in traditional models and visualization improvement models.

REFERENCES

- [1] W. J. Moy, G. Ma, K. M. Kelly and B. Choi, "Hemoporphyrin-mediated photodynamic therapy on normal vasculature: implications". *Journal of clinical and translational research*, vol. 2, no. 3, pp. 107, 2016.
- [2] A. Y. Neganova, D. D. Postnov, O. Sosnovtseva, J. C. B. Jacobsen, "Rat retinal vasomotion assessed by laser speckle imaging". *PLoS one*, vol. 12, no. 3, pp. e0173805, 2016.
- [3] A. Cho, C. Yeon, D. Kim, and E. Chung, "Laser speckle contrast imaging for measuring cerebral blood flow changes caused by electrical sensory stimulation". *Journal of the Optical Society of Korea*, vol. 20, no. 1, pp. 88-93, 2016.
- [4] D. A. Boas, and A. K. Dunn, "Laser speckle contrast imaging in biomedical optics". *Journal of biomedical optics*, vol. 15, no. 1, pp. 011109, 2010.
- [5] D. Briers, D. Duncan, S. Kirkpatrick, M. Larsson, T. Stromberg, and O. Thompson, "Laser speckle contrast imaging: Theoretical and practical limitations". *Journal of biomedical optics*, vol. 18, no. 6, pp. 1-9, 2013.
- [6] Y. A. Aizu and T. Asakura, "Bio-speckle phenomena and their application to the evaluation of blood flow". *Optics & Laser Technology*, vol. 23, no. 4, pp. 205-219, 1991.
- [7] M. Draijer, E. Hondebrink, T. van Leeuwen, and W. Steenbergen, "Review of laser speckle contrast techniques for visualizing tissue perfusion". *Lasers in medical science*, vol. 24, no. 6, pp. 639, 2019.
- [8] D. D. Duncan and S. J. Kirkpatrick, "Can laser speckle flowmetry be made a quantitative tool?". *Journal of the Optical Society of America*, vol. 25, no. 8, pp. 2088-2094, Aug. 2008.
- [9] P. G. Vaz, A. Humeau-Heurtier, E. Figueiras, C. Correia, and J. Cardoso, "Laser speckle imaging to monitor microvascular". *IEEE reviews in biomedical engineering*, vol. 9, pp. 106-120, 2016.
- [10] T. Son, J. Lee, and B. Jung, "Contrast enhancement of laser speckle contrast image in deep vasculature by reduction of tissue scattering". *Journal of the Optical Society of Korea*, vol. 17, no. 1, pp. 86-90, 2013.
- [11] J. Kim, J. Oh, B. Choi, "Magnetomotive laser speckle imaging". *Journal of biomedical optics*, vol. 15, no. 1, pp. 011110, 2010.
- [12] C. Regan, J. C. Ramirez-San-Juan, B. Choi, "Photothermal laser speckle imaging". *Optics letters*, vol. 39, no. 17, pp. 5006-5009, 2014.
- [13] Y. Wang, D. Wen, X. Chen, Q. Huang, M. Chen, J. Lu, and P. Li, "Improving the estimation of flow speed for laser speckle imaging with single exposure time". *Optics letters*, vol. 42, no. 1, pp. 57-60, 2017.
- [14] J. D. Briers and S. Webster, "Laser speckle contrast analysis (LASCA): a non-scanning, full-field technique for monitoring capillary blood flow". *Journal of biomedical optics*, vol. 1, no. 2, pp. 174-180, 1996.
- [15] H. Peregrina-Barreto, E. Perez-Corona, J. Rangel-Magdaleno, R. Ramos-Garcia, R. Chiu and J. C. Ramirez-San-Juan, "Use of kurtosis for locating deep blood vessels in raw speckle imaging using a homogeneity representation". *Journal of biomedical optics*, vol. 22, no. 6, pp. 066004, 2017.
- [16] C. Perez-Corona, H. Peregrina-Barreto, J. Rangel-Magdaleno, R. Ramos-Garcia, and J. Ramirez-San-Juan, "Spacedirectional laser speckle contrast imaging to improve blood vessels visualization". In *2018 IEEE International Instrumentation and Measurement Technology Conference (I2MTC)* pp. 1-5, May, 2018.
- [17] K. Basak, G. Dey, M. Mahadevappa, M. Mandal, and P. K. Dutta, "In vivo laser speckle imaging by adaptive contrast computation for microvasculature assessment". *Optics and Lasers in Engineering*, vol. 62, pp. 87-94, 2014.
- [18] A. Rege, J. Senarathna, N. Li, and N. V. Thakor, "Anisotropic processing of laser speckle images improves spatiotemporal resolution". *IEEE Transactions on Biomedical Engineering*, vol. 59, no. 5, pp. 1272-1280, 2012.
- [19] J. A. Arias-Cruz, R. Chiu, H. Peregrina-Barreto, R. Ramos-Garcia, T. Spezzia-Mazzocco, and J. C. Ramirez-San-Juan, "Visualization of in vitro deep blood vessels using principal component analysis based laser speckle imaging". *Biomedical optics express*, vol. 10, no. 4 pp. 2020-2031, 2019.
- [20] E. B. Postnikov, M. O. Tsoy, and D. E. Postnov, "Matlab for laser speckle contrast analysis (lasca): a practice-based approach". *Saratov Fall Meeting 2017: Laser Physics and Photonics XVIII; and Computational Biophysics and Analysis of Biomedical Data IV. International Society for Optics and Photonics*, vol. 10717, pp. 1071728, 2018.
- [21] E. Morales-Vargas, J. Sosa-Martinez, H. Peregrina-Barreto, J. Rangel-Magdaleno and J. C. Ramirez-San-Juan, "A morphological approach for locating blood vessels in laser contrast speckle imaging". In *2018 IEEE International Instrumentation and Measurement Technology Conference (I2MTC)*, pp. 1-6, May, 2018.
- [22] E. Morales-Vargas, H. Peregrina-Barreto, J. Rangel-Magdaleno and J. C. Ramirez-San-Juan, "Estimation of blood vessels diameter by region growing in laser speckle contrast imaging". In *2019 IEEE International Instrumentation and Measurement Technology Conference (I2MTC)* pp. 1-5, May, 2019.
- [23] F. Lopez-Tiro, H. Peregrina-Barreto, J. Rangel-Magdaleno and J. C. Ramirez-San-Juan, "Visualization of in-vitro Blood Vessels in Contrast Images Based on Discrete Wavelet Transform Decomposition". In *2019 IEEE International Instrumentation and Measurement Technology Conference (I2MTC)* pp. 1-6, May, 2019.
- [24] D. D. Postnov, V. V. Tuchin, and O. Sosnovtseva, "Estimation of vessel diameter and blood flow dynamics from laser speckle images". *Biomedical optics express*, vol. 7, no. 7, pp. 2759-2768, 2016.
- [25] R. B. Saager, C. Kondru, K. Au, K. Sry, F. Ayers, and A. J. Durkin, "Multilayer silicone phantoms for the evaluation of quantitative optical techniques in skin imaging". *International Society for Optics and Photonics*, vol. 7567, pp. 756-706, 2010.
- [26] M. Kimlyk, and S. V. Umnyashkin, "Image denoising using discrete wavelet transform and edge information". In *2018 IEEE 57 Conference of Russian Young Researchers in Electrical and Electronic Engineering (EIConRus)*, pp. 1823-1825, 2018.
- [27] S. Agarwal, O. P. Singh, and D. Nagaria, "Analysis and Comparison of Wavelet Transforms For Denoising MRI Image". *Biomedical and Pharmacology Journal*, vol. 10, no. 2, pp. 831-836, 2017.
- [28] L. Feng and L. Lin, "Image Denoising Methods Based on Wavelet Transform and Threshold Functions". *JMPT*, vol. 8, pp. 1-10, 2017.
- [29] S. G. Mallat, "A wavelet tour of signal processing". *Elsevier*, 2008.
- [30] M. J. Shensa, "The discrete wavelet transform: wedding the a trous and mallat algorithms". *IEEE Trans. Signal Processing*, vol. 40, pp. 2464-2482, 1992.
- [31] I. Daubechies, and J. C. Bates, "Ten lectures on wavelets", 1993.
- [32] N. Dhanachandra, K. Manglem and Y. J. Chanu, "Image segmentation using K-means clustering algorithm and subtractive clustering algorithm". *Procedia Computer Science*, vol. 54, pp. 764-771, 2015.